Energy & Environmental Science

ROYAL SOCIETY OF CHEMISTRY

PAPER

View Article Online
View Journal

Cite this: DOI: 10.1039/c9ee02657f

Stabilizing atomic Pt with trapped interstitial F in alloyed PtCo nanosheets for high-performance zinc-air batteries†

Zhao Li,‡[ab] Wenhan Niu,‡[b] Zhenzhong Yang,‡[c] Nusaiba Zaman,[d] Widitha Samarakoon,[e] Maoyu Wang,[e] Abdelkader Kara,[d] Marcos Lucero,[e] Manasi V. Vyas,[e] Hui Cao,[f] Hua Zhou,[g] George E. Sterbinsky,[g] Zhenxing Feng,*[e] Yingge Du*[c] and Yang Yang*[abh]

Received 4th June 2019,
Accepted 22nd November 2019

DOI: 10.1039/c9ee02657f

rsc.li/ees

Recently, considerable attention has been paid to the stabilization of atomic platinum (Pt) catalysts on desirable supports in order to reduce Pt consumption, improve the catalyst stability, and thereafter enhance the catalyst performance in renewable energy devices such as fuel cells and zinc-air batteries (ZABs). Herein, we rationally designed a novel strategy to stabilize atomic Pt catalysts in alloyed platinum cobalt (PtCo) nanosheets with trapped interstitial fluorine (SA-PtCoF) for ZABs. The trapped interstitial F atoms in the PtCoF matrix induce lattice distortion resulting in weakening of the Pt–Co bond, which is the driving force to form atomic Pt. As a result, the onset potentials of SA-PtCoF are 0.95 V and 1.50 V for the oxygen reduction and evolution reactions (ORR and OER), respectively, superior to commercial Pt/C@RuO_2. When used in ZABs, the designed SA-PtCoF can afford a peak power density of 125 mW cm^{-2} with a specific capacity of 808 mA h g_{Zn}^{-1} and excellent cyclability over 240 h, surpassing the state-of-the-art catalysts.

Broader context

A new strategy for the scalable and repeatable synthesis of atomic Pt in alloyed platinum cobalt (PtCo) nanosheets is designed by combining bottom-up electrodeposition and top-down fluorine-plasma (F-plasma) etching treatments. The interstitial F atoms trapped in the alloyed PtCo crystal structure induce lattice distortion which plays a crucial role in stabilizing the atomic Pt on the surface of the catalyst (denoted as SA-PtCoF) by balancing the surface free energy. Moreover, the proposed SA-PtCoF nanosheets are additive-free catalysts with abundant active sites and high surface area, which show significant advantages over powder catalysts for Zn-air batteries (ZABs) due to the suppressed catalyst deactivation. Benefiting from the catalyst–support interactions and synergistic effects of SA-PtCoF, an unprecedented ZAB performance (power density of 125 mW cm^{-2}, capacity of 808 mA h g_{Zn}^{-1}, cycle life over 240 h) is achieved, superior to commercial Pt/C@RuO_2 and other state-of-the-art ORR/OER catalysts.

1. Introduction

Driven by the ever-increasing demand for zero-emission technologies, emerging renewable energy devices such as hydrogen fuel cells and metal–air batteries have been extensively explored. Among various new technologies in the field of energy conversion and storage, a rechargeable zinc-air battery (ZAB) is considered as a promising candidate due to its high energy density, reliability, and low cost.[1] However, its practical application has been severely impeded by the sluggish four-electron transfer kinetics of the oxygen reduction and evolution reactions (ORR and OER). Meanwhile, a ZAB suffers from the poor cyclability caused by different catalyst deactivation mechanisms, such as catalyst aggregation, corrosion, and surface passivation in alkaline electrolytes.[1–3] Platinum group metals (PGMs) and

[a] Department of Materials Science and Engineering, University of Central Florida, Orlando, FL 32826, USA. E-mail: Yang.Yang@ucf.edu
[b] NanoScience Technology Center, University of Central Florida, Orlando, FL 32826, USA
[c] Physical and Computational Sciences Directorate, Pacific Northwest National Laboratory, Richland, Washington 99352, USA. E-mail: Yingge.Du@pnnl.gov
[d] Department of Physics, University of Central Florida, Orlando, FL 32826, USA
[e] School of Chemical, Biological, and Environmental Engineering, Oregon State University, Corvallis, OR 97331, USA. E-mail: zhenxing.feng@oregonstate.edu
[f] Materials Science Division, Argonne National Laboratory, Lemont, IL 60439, USA
[g] X-ray Science Division, Argonne National Laboratory, Lemont, IL 60439, USA
[h] Energy Conversion and Propulsion Cluster, University of Central Florida, Orlando, FL 32826, USA

† Electronic supplementary information (ESI) available: Materials and electrochemical characterizations. See DOI: 10.1039/c9ee02657f

‡ These authors contributed equally to this work.

their corresponding compounds, including Pt, Ru, and Ir-based materials, are still dominantly used as ORR/OER electrocatalysts because of their favorable surface electronic structures for electrochemical reactions.[1,4–6] However, their high cost and scarcity prevent their large-scale application in ZABs. A great variety of PGM-free catalysts including functional carbon materials, transition metal-based materials, and their composites have been recently developed as a promising strategy for high-efficiency ZABs.[2,3,7] However, their activity and stability still could not meet the industrial demands for practical applications.

Another strategy is to rationally design stable and low-PGM ORR/OER catalysts stabilized in conducting host materials, which can reduce the PGM consumption and meanwhile improve the utilization efficiency of PGMs. To this end, several strategies have been employed, for instance, alloying PGMs with inexpensive transition metals and reducing PGM particle size down to the cluster or even single-atom level.[8,9] Among these strategies, anchoring atomic PGMs on conducting supports has been recognized as the most effective way to synthesize low-PGM catalysts. Because of the abundant active sites derived from the low coordination and unsaturated chemical environment, these atomic PGM catalysts show superior catalytic activity to commercial PGM particles.[10] Nevertheless, atomic PGMs supported on metal oxide and carbon supports cannot meet the stringent requirements for high-performance ZABs, due to either the poor conductivity of oxides or instability of carbons under strong oxidative polarization and harsh alkaline conditions.[11–13] Motivated by recent progress in transition metal alloys for high-efficiency electrocatalytic reactions,[14–19] alloyed nanomaterials are considered as ideal candidates to stabilize atomic PGMs not only because of their remarkable conductivities and high corrosion resistance but also due to the beneficial catalyst–support interactions and synergistic effects caused by a potential charge transfer between the PGM and the alloyed metals. However, traditional synthetic approaches to atomic catalysts, such as wet impregnation and atomic layer deposition, still have a long way to be optimized for industrial mass production.[20]

Plasma treatment under different atmospheres, such as O_2, N_2, and Ar, has traditionally been used to clean materials surfaces by etching the naturally formed surface oxide/hydroxide layers and carbonaceous contamination.[21,22] Consequently, structural voids can be created to expose more surface area if the plasma treatment is properly controlled. However, how to tune the chemical compositions of materials by plasma and how to integrate plasma treatment with other materials processing techniques in order to design new materials are still not well understood. Herein, we propose a novel strategy by combining bottom-up electrodeposition and top-down fluorine-plasma (F-plasma) etching treatment to stabilize atomic platinum (Pt) in alloyed platinum cobalt (PtCo) nanosheets. The interstitial F atoms trapped in the alloyed PtCo (denoted as PtCoF) crystal structure induce lattice distortion[23] which plays a crucial role in stabilizing the atomic Pt on the surface of PtCoF (denoted as SA-PtCoF) by balancing the surface free energy.[24,25] Moreover, the proposed SA-PtCoF nanosheets are additive-free catalysts with abundant active sites and high surface area, which show significant advantages over powder catalysts for ZABs due to the suppressed catalyst deactivation such as catalyst aggregation, active site poisoning, and gas/electrolyte diffusion pathway blocking in powder materials. In addition, the proposed SA-PtCoF catalysts have improved electronic conductivity by tuning the charge and spin density of atoms, contributing to the enhanced electrocatalytic activity in ZABs.[26,27] Benefiting from the catalyst–support interactions and synergistic effects of SA-PtCoF, bifunctional ORR/OER catalysts with unprecedented activity and durability for ZABs are rationally developed, which show superior performance to commercial Pt/C@RuO_2 and other state-of-the-art ORR/OER catalysts.

2. Results and discussion

The synthetic procedure for SA-PtCoF and the atomic model of the catalyst surface layer are schematically illustrated in Fig. 1a and Fig. S1 (ESI†), respectively. Firstly, PtCo was fabricated through a bottom-up electrodeposition process using nickel foam as a substrate in an aqueous plating solution composed of a fixed amount of cobalt sulfide and various concentrations of chloroplatinic acid (H_2PtCl_6). The rationale for using nickel foam as a substrate is that its 3D porous microstructure provides high surface area for the efficient loading of active materials in electrochemical devices, and it has been widely used in the applications of metal–air batteries.[28–30] It should be noted that ''PtCo'' used in this work does not mean the stoichiometric Pt/Co ratio of 1. The actual atomic ratios of elements were determined by X-ray fluorescence (XRF). By controlling the concentration of H_2PtCl_6, an ultralow amount of Pt was alloyed with Co, forming PtCo nanosheets. Then, PtCo was treated by a top-down F-plasma etching process, leading to the increased surface roughness of nanosheets. Meanwhile, F atoms were trapped in the interstitial sites of the PtCo crystal structure which significantly affected the surface free energy. Thermodynamically driven by the trapped interstitial F, the Pt–Co bond will be weakened, consequently leading to the diffusion and stabilization of Pt atoms on PtCoF nanosheet edges. Eventually, SA-PtCoF was directly used as an additive-free and bifunctional ORR/OER catalyst for ZABs without any further treatment.

Scanning electron microscopy (SEM) and aberration-corrected scanning transmission electron microscopy (STEM) were utilized to investigate the morphology and composition of SA-PtCoF. As illustrated in Fig. 1b and Fig. S2a (ESI†), after F-plasma etching, SA-PtCoF nanosheets with rough surfaces and exposed edges were vertically grown on the nickel foam. By contrast, PtCo without F-plasma treatment shows a smooth surface (Fig. S2b, ESI†). It should be noted that a naturally formed thin ($\sim$20 nm, Fig. S2c and d, ESI†) hydroxylated Co layer on the nanosheets was easily etched by F-plasma treatment, creating tiny holes and forming rough surfaces.[20] The atomic structure of SA-PtCoF was studied by aberration-corrected atomic-resolution annular bright-field (ABF) and high-angle annular dark-field (HAADF) STEM. With the advantage of ABF-STEM, in which the image contrast

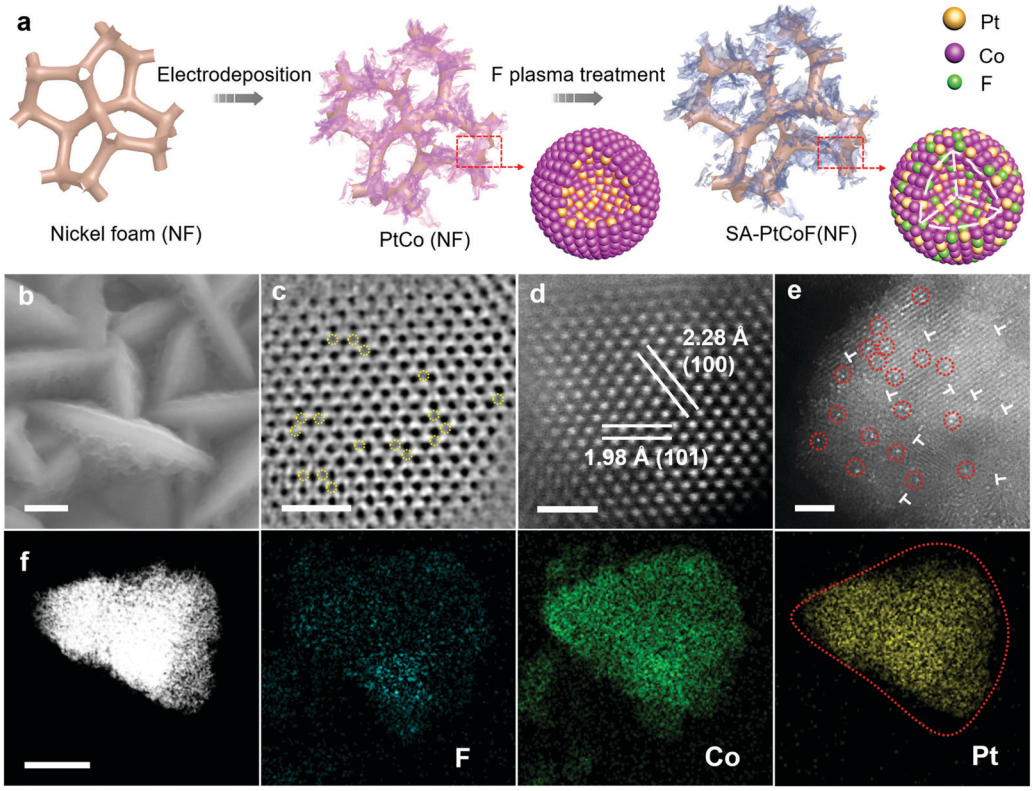

Fig. 1 Morphology and atomic structure of SA-PtCoF nanosheets. (a) Schematic illustration of the fabrication process for SA-PtCoF nanosheets. (b) SEM image of SA-PtCoF nanosheets vertically grown on nickel foam. Scale bar, 200 nm. (c and d) ABF-STEM and HAADF-STEM images of SA-PtCoF. The yellow dashed circles represent the interstitial F atoms. Scale bar, 1 nm. (e) HAADF-STEM images of SA-PtCoF with incorporated lattice distortions. The isolated Pt atoms and lattice distortions are marked by red cycles and "T", respectively. Scale bar, 2 nm. (f) STEM-EDS elemental mapping of SA-PtCoF. Scale bar, 50 nm.

exhibits a $\sim Z^{1/3}$ dependence with respect to the atomic number Z, both the light and heavy atoms can be observed simultaneously. Therefore, the interstitial F atoms can be identified from the PtCo lattice fringe, marked by yellow dashed circles in the ABF-STEM image (Fig. 1c). The lattice fringes of SA-PtCoF show spacings of 1.98 Å and 2.28 Å (Fig. 1d), corresponding to the (101) and (100) planes of Co alloyed with a trace amount of Pt, respectively. The lattice distortion caused by the trapped interstitial F is identified by the slight difference between the lattice spacings. As clearly shown in the HAADF-STEM images (Fig. 1e and Fig. S3a, ESI†), the isolated Pt atoms (marked by red circles) were formed on the edges of nanosheets surrounding the lattice distortions (marked by "T"). Meanwhile, the PtCoF matrix of SA-PtCoF is imperfect with lattice distortions as shown in Fig. S4a (ESI†). For comparison, the PtCo alloy without F-plasma treatment (no trapped interstitial F in the crystal structure) does not present atomic Pt on the nanosheet surfaces (Fig. S3b, ESI†) and its corresponding matrix shows perfect and unaffected lattice fringes (Fig. S4b, ESI†). Therefore, we suggest that the interstitial F atoms are thermodynamically metastable, pushing Pt atoms outwards from the PtCoF crystal structure by weakening the Pt–Co bond, and eventually forming isolated Pt atoms on the edges of the distorted PtCoF nanosheets in order to achieve a stable state by decreasing the surface free energy. As a consequence, the sufficiently exposed atomic Pt on the catalyst surface will improve the utilization efficiency of Pt in the ultralow-Pt-loaded materials towards high-performance ZABs.

Elemental distributions of PtCo and SA-PtCoF (before and after F-plasma treatment, respectively) were characterized by STEM-energy dispersive spectroscopy (EDS) element mapping (Fig. S5 (ESI†) and Fig. 1f). Without F-plasma treatment, Co and Pt were uniformly distributed across the whole PtCo nanosheets (Fig. S5, ESI†), indicating a controllable synthesis of PtCo using bottom-up electrodeposition. However, SA-PtCoF nanosheets show uniform distributions of Co and F after F-plasma treatment in the elemental mapping images (Fig. 1f). On the other hand, the lack of Pt signals outlined by the red dashed circle as compared with the obvious Pt distribution in PtCo indicates the atomically dispersed Pt in SA-PtCoF. It is consistent with the fact that an ultralow Pt content was observed at the edges of SA-PtCoF nanosheets as observed in HAADF-TEM (Fig. 1e and Fig. S3a, ESI†), further confirming the formation of atomic Pt in the PtCoF matrix. Moreover, PtCoF catalysts with different Pt weight percentages (*i.e.*, 0 wt%, 1.85 wt%, and 6.21 wt% detected by XRF) were prepared and characterized using the same procedure as that used for SA-PtCoF (5.86 wt%). PtCoF with 1.85 wt% and 6.21 wt% Pt and CoF (0 wt% Pt) nanosheets suffer from similar morphology destruction and surface roughness increase after F-plasma treatment as shown in the SEM images (Fig. S6, ESI†). Instead of forming individually isolated Pt single atoms,

severely aggregated Pt nanoclusters were detected on PtCoF nanosheets with 6.21 wt% Pt (denoted as NC-PtCoF) as shown in the HAADF-STEM image (Fig. S7a, ESI†). It should also be noted that NC-PtCoF shows a greatly destroyed surface morphology after F-plasma treatment, indicating the poorly maintained structural integrity in the catalyst with high Pt loading. It is definitely unfavorable for enhancing the catalytic performance using catalysts with high Pt loading and a severely cracked structure. On the other hand, upon decreasing the Pt loading amount to 1.85 wt% (denoted as AP-PtCoF), Pt was mostly detected in the alloy phase of PtCoF nanosheets as highlighted by red dashed circles in Fig. S7b (ESI†), indicating that Pt loading is too low to form atomically dispersed single atoms. In short, a Pt loading of 5.86 wt% is optimal to stabilize the atomic Pt on the alloyed PtCoF matrix, which is favorable for maximal exposure of active Pt sites.

The crystal structures of Co, CoF, PtCo, and SA-PtCoF were identified by X-ray diffraction (XRD, Fig. 2a). Three main characteristic peaks located at 41.55°, 44.55° and 47.45° correspond to the (100), (002) and (101) planes of hcp-Co (JCPDS No. 89-7373), respectively, which agree well with TEM observations.[31,32] However, the diffraction peak belonging to Pt is absent due to the ultralow Pt loading. Moreover, the diffraction peaks of CoF, PtCo, and SA-PtCoF slightly shift to lower angles as compared with Co, which is due to the lattice distortion and strain induced by the incorporation of Pt and F atoms.[33]

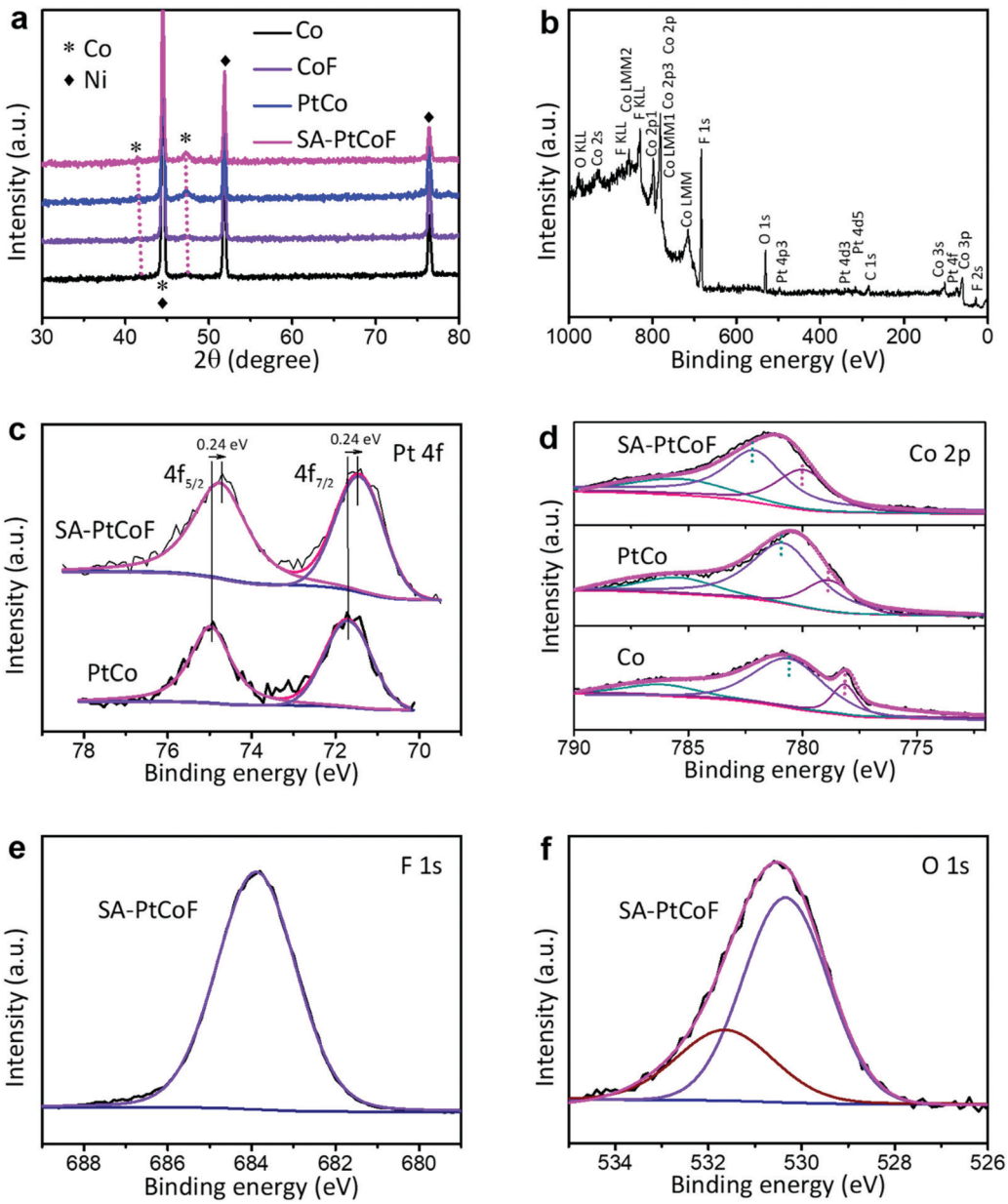

Fig. 2 Structural and compositional characterizations. (a) XRD patterns of SA-PtCoF and control catalysts (Co, CoF, and PtCo). (b) XPS full-spectrum and the corresponding high-resolution XPS spectra of (c) Co 2p, (d) Pt 4f, (e) F 1s, and (f) O 1s of SA-PtCoF.

The chemical states and compositions of SA-PtCoF and other control samples were studied by X-ray photoelectron spectroscopy (XPS). The XPS survey spectrum (Fig. 2b) confirms the existence of Co, Pt, F, and O in SA-PtCoF. It should be noted that the naturally formed surface hydroxylated Co layer was etched by F-plasma treatment, which is proved by the significantly reduced O content in the plasma-treated samples (Fig. S8, ESI†). The high-resolution XPS Pt 4f peaks of SA-PtCoF located at 71.48 eV and 74.72 eV belong to metallic Pt (Fig. 2c). More importantly, the binding energy of Pt in SA-PtCoF slightly decreases by 0.24 eV and 0.90 eV as compared with PtCo and commercial Pt/C shown in Fig. S9 (ESI†), respectively, indicating a strong interaction between the atomic Pt and the alloyed PtCoF matrix.[20] Such a decrease in the XPS Pt core binding energy reveals the downshift of the d-band center relative to the Fermi level, attributing to the weakened adsorption of oxygen species on the atomic Pt.[34] Consequently, a facilitated charge transfer could be achieved during catalytic reactions.[35] The increased Pt content from 4.37 wt% in PtCo to 5.81 wt% in SA-PtCoF after F-plasma treatment indicates the diffusion and stabilization of Pt atoms on the nanosheet surface driven by the trapped interstitial F atoms. Three fitted XPS Co $2p_{3/2}$ peaks of SA-PtCoF located at 779.9 eV, 781.9 eV, and 785.8 eV are ascribed to Co^0, Co^{2+}, and the satellite (Fig. 2d),[36,37] which show increased binding energies as compared with Co and PtCo because of the influence of d-band reactivity and the strong electronegativity of the trapped interstitial F.[16] Here, Co acting as an electron-donating center may transfer electrons to the adjacent Pt atoms and therefore enhance the electrocatalytic performance of SA-PtCoF.[38] Moreover, two fitted XPS O 1s peaks (Fig. 2f) at 530.4 eV and 531.6 eV are assigned to the surface absorbed hydroxyl groups and oxygen, which are crucial for creating a hydrophilic surface for oxygen electrocatalytic reactions.[36,39,40] The XPS F 1s peak of SA-PtCoF located at 683.9 eV belongs to the Co–F bond,[41,42] which confirms the trapped F atoms in PtCo.

In order to determine the extent of insertion of F atoms into PtCo, we performed density functional theory (DFT) calculations for a bulk CoPt supercell with and without the F atom placed in an interstitial site near the Pt atom. The corresponding atomic structural model along the *c*-axis is shown in Fig. S10 (ESI†) and the molar ratio of Co/Pt (53 : 1) agrees well with that in SA-PtCoF. We used density functional theory as implemented in the Vienna Ab initio Simulation Package (VASP) code.[43] Spin-polarized calculations were performed using the generalized gradient approximation of the Perdew–Burke–Ernzerhof (PBE) exchange–correlation functionals,[44] where the interaction between the valence electrons and ionic cores was described by the projector augmented wave (PAW) method.[45] A plane-wave basis set including waves with an energy cutoff of 400 eV was used throughout the calculations.

We first calculated the lattice parameters of bulk Co which are a = 2.45 Å and c = 3.95 Å; these values are close to the experimental values (a = 2.51 Å and c = 4.07 Å).[46] For a Pt atom to migrate from the bulk Co environment to the surface, the bonding with its neighbors in the bulk should weaken. In this case, the phonons (vibrational density of states) of the system should show a softening, or shift towards low frequencies, when F atoms are introduced near Pt atoms. In the present case, when an F atom is inserted, the nearest neighbor distance between the Pt atom and its Co atoms increased from 2.49 Å to an average of 2.59 Å (Table S1, ESI†), resulting from an anisotropic distortion near the Pt atom (Fig. 3a and b). When calculating the vibrational frequencies where only the Pt atom is allowed to oscillate, its vibrational frequencies changed from 5.32 THz, 5.32 THz and 5.06 THz to 4.85 THz, 4.19 THz and 4.10 THz, when an F atom was inserted, as shown in Table S2 (ESI†). This is a substantial shift towards low frequencies, reflecting the weakening of the Pt bond to its neighboring Co atoms when an F atom is inserted.

To further prove this conclusion, we have allowed Pt and its first nearest neighbors (including F atom, when inserted) to oscillate. In Fig. S11 (ESI†), we show the calculated vibrational density of states (VDOS) in the absence and presence of an F atom. It is clear that there is a substantial softening of the vibrational modes resulting from a weakening of the Co–Pt bond at a low frequency. The modes at higher frequencies correspond to vibrational modes associated solely with the F atom and its neighboring Co atoms without involving the Pt atom, which reflects a stiff F–Co bond as well as a weakened Co–Pt bond. Thus, it clearly illustrates that interstitial F atoms play an important role in weakening the Co–Pt bond and contributing to free Pt atoms on the surface of nanosheets with low energy barriers.

X-ray absorption spectroscopy (XAS) was performed to understand the effect of F-plasma treatment on the oxidation state and local structure of SA-PtCoF.[47–51] The comparison of Co K-edge X-ray absorption near edge structure (XANES) spectra of SA-PtCoF and PtCo with Co show that Co is in the metallic state in both SA-PtCoF and PtCo samples (Fig. 3c), which is further verified by the similarity in the first derivative of the normalized absorbance (Fig. S12a, ESI†). Co K-edge extended X-ray absorption fine structure (EXAFS) fitting for SA-PtCoF and PtCo reveals that Co–Co coordination is predominant in both samples (Fig. 3d and Fig. S12b, ESI†). This suggests that the local coordination environment of Co in both samples consists almost entirely of Co atoms from the PtCo alloy, which could be due to the low loading of Pt in both samples. EXAFS results are also supported by the evidence of the lack of a diffraction peak for Pt in XRD. The Pt L_3-edge spectrum of SA-PtCoF is similar to that of PtCo (Fig. 3e). Pt L_3-edge EXAFS fitting results for SA-PtCoF and PtCo in both *R*-space (Fig. 3f) and *k*-space (Fig. S12c, ESI†) show Pt–Co coordination in both samples but no Pt–Pt coordination. This can also be attributed to the ultralow loading of Pt in both samples. Pt–Co bond lengths in SA-PtCoF and PtCo are 2.562 Å and 2.554 Å respectively (Table S3, ESI†). This slight increase of Pt–Co bond length may be a result of the weakening of the Pt–Co bond in the PtCo alloy as the thermodynamically metastable interstitial F atoms tend to push Pt atoms outwards from the alloy. This finding agrees with DFT calculation results and HAADF-STEM imaging results as well. This can be further elucidated by comparing the first peak amplitudes (at phase-uncorrected $R \sim 2.2$ Å) in Pt L_3-edge Fourier-transformed EXAFS spectra and the calculated

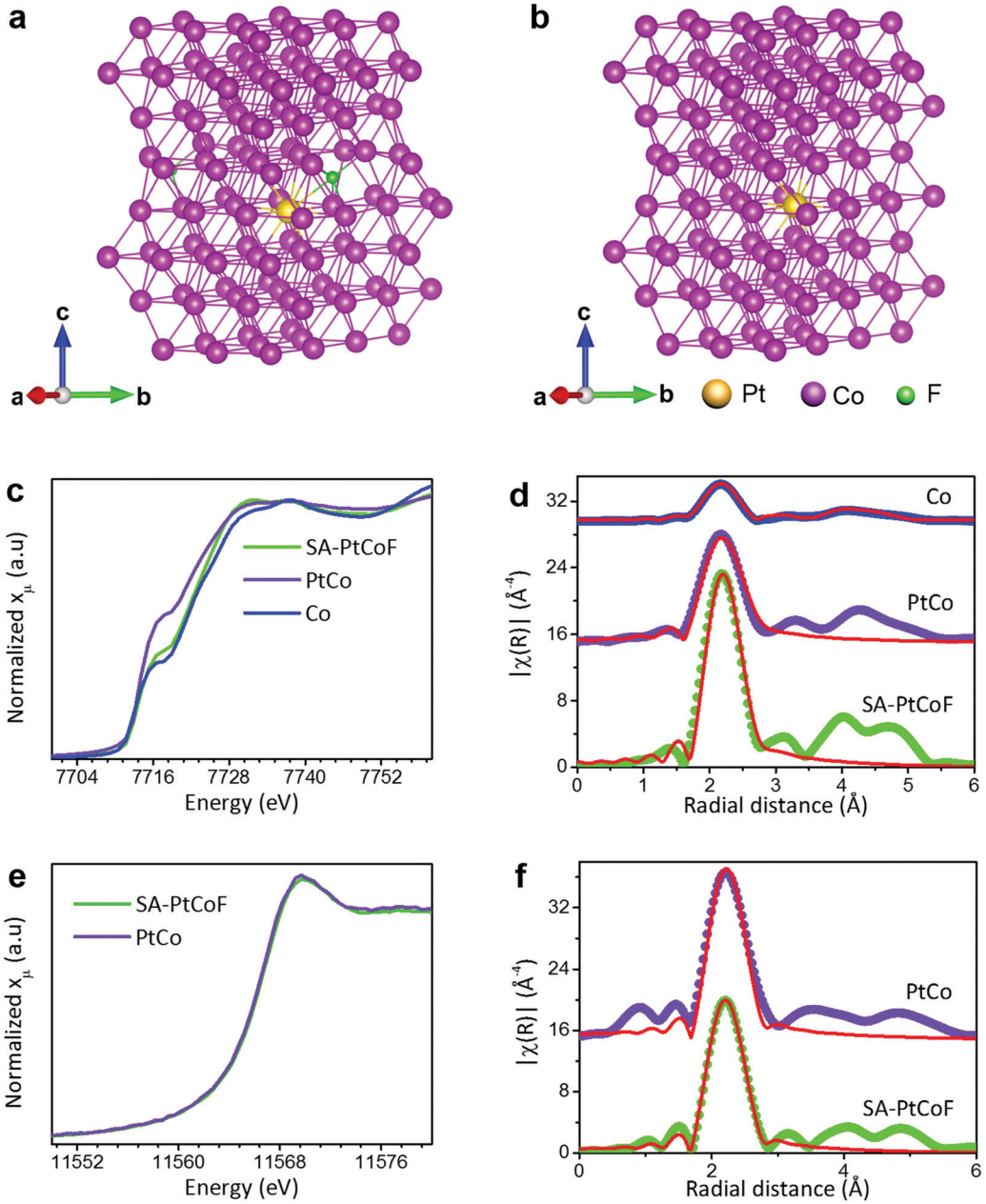

Fig. 3 Computational and experimental studies of structural changes in SA-PtCoF and PtCo. Atomic structure model of (a) PtCoF and (b) PtCo, highlighting the anisotropic bond near single atomic Pt. (c) XANES Co K-edge spectra for SA-PtCoF and PtCo. (d) EXAFS Co K-edge fitting results for SA-PtCoF, PtCo, and Co. (e) XANES Pt L_3-edge spectra for SA-CoPtF and PtCo. (f) EXAFS Pt L_3-edge fitting results for SA-CoPtF and PtCo. For graphs d and f, circles represent the data and the solid red line represents the fit.

coordination numbers for the Pt–Co bond and the Co–Co bond in Pt and Co EXAFS spectra. The peak amplitude and coordination number (Table S3, ESI†) for the first shell Pt–Co bond in SA-CoPtF are lower than those in PtCo. This difference may be caused by the presence of isolated single Pt atoms ejected from the alloy phase in addition to the Pt already existing in the alloy phase in SA-PtCoF. Since the isolated Pt atoms tend to show minimal coordination with neighboring atoms when compared to Pt in the alloy, the final coordination number calculated will be reduced on average, ultimately leading to a lower coordination number for the Pt–Co bond in SA-CoPtF. In contrast, the coordination number for the first shell Co–Co bond in SA-CoPtF (9.5) from Co K-edge EXAFS spectra is higher than that in PtCo (6.0) (Table S3, ESI†). This can also be explained by the fact that ejecting Pt atoms from the alloy in SA-PtCoF causes the neighboring Co atoms to reorganize in a manner so that some of them occupy the vacancies left by the ejected Pt atoms, thereby increasing the coordination number. Both these provide evidence to support the effect of interstitial F in weakening the Pt–Co bond in the alloy and formation of isolated Pt atoms in SA-PtCoF and thereby increasing the catalytic activity.

Electrochemical analyses were conducted on SA-PtCoF and other control catalysts to investigate the structure–property

relationships. ORR and OER activities were measured by a standard three-electrode setup in 1 M KOH. Firstly, to evaluate the ORR performance, cyclic voltammograms (CVs) were recorded in N_2- and O_2-saturated electrolytes at a scan rate of 5 mV s^{-1} (Fig. S13, ESI†). All catalysts except pure Co show an obvious oxygen reduction peak in the O_2-saturated solution. As compared with the bare Co catalyst without any further treatment, the reduction peaks and onset potentials for the CoF, PtCo, and SA-PtCoF catalysts successively have positive shifts, indicating the enhanced ORR activity by F and Pt atom incorporation. Among all catalysts, SA-PtCoF exhibits the most positively shifted onset potential and ORR peak, revealing the greatly enhanced ORR activity. Thus, it further confirms that the atomic Pt stabilized in the PtCoF matrix with low coordination and an unsaturated configuration plays an important role in enhancing the ORR activity.[20] Furthermore, linear sweep voltammetry (LSV) curves examined in O_2-saturated 1 M KOH also show that SA-PtCoF displays the optimum ORR performance with a more positive onset potential of 0.95 V as compared with 0.87 V for Co, 0.9 V for CoF, 0.92 V for PtCo, which is also very competitive to 0.96 V for Pt/C@RuO_2 catalysts (Fig. 4a). It suggests a potential electron transfer and synergistic effects between the atomic Pt and the surrounding alloyed support. Specifically, after trapping interstitial F in the PtCo crystal structure, the atomic Pt is stabilized in the alloyed matrix with a favorable electronic structure for rapid electron transfer and O_2 reduction.[35] Half-wave potentials ($E_{1/2}$) of SA-PtCoF is about 0.88 V, which is evidently higher than those of Co (0.68 V), CoF (0.74 V), and PtCo (0.86 V). Meanwhile, a much higher limiting current density of 5.79 mA cm^{-2} at a potential

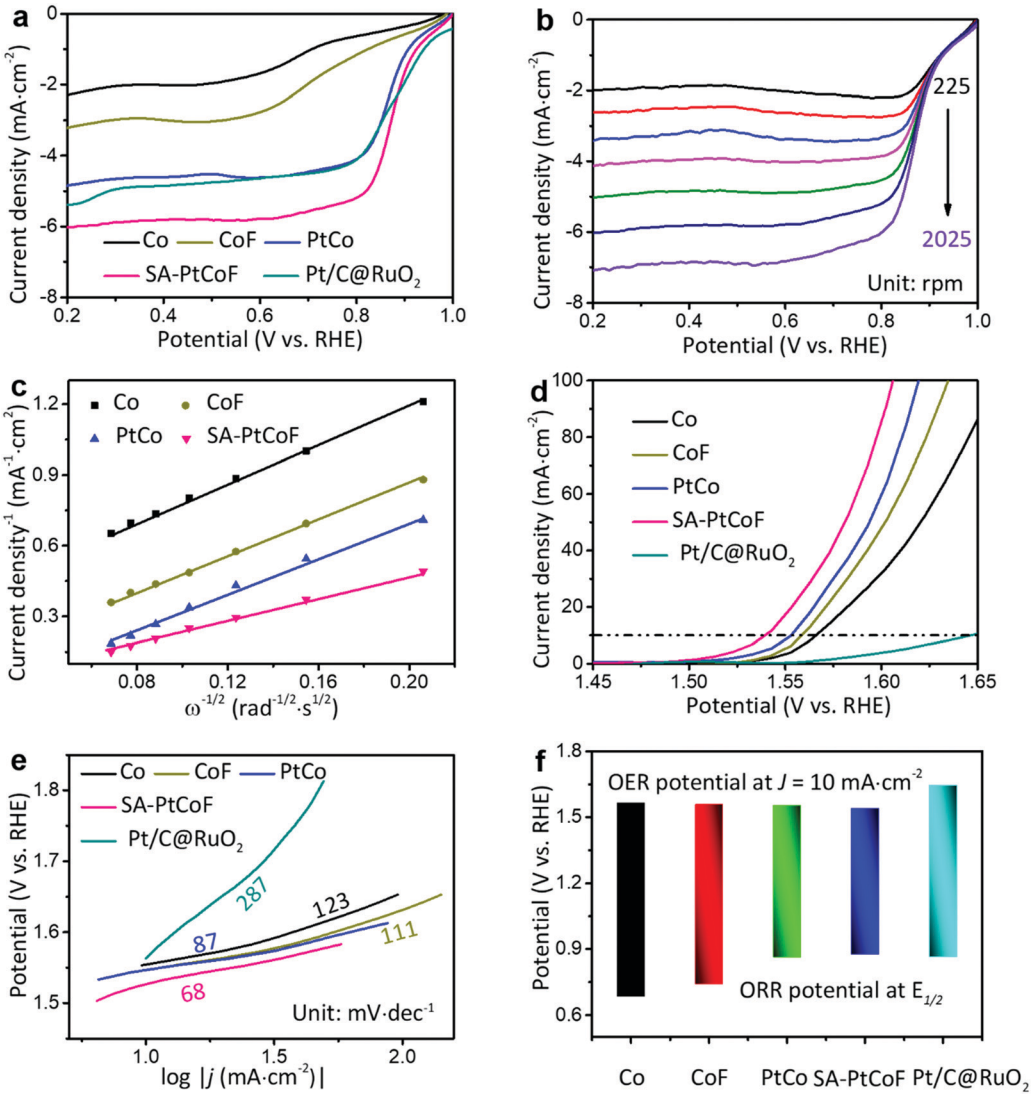

Fig. 4 ORR and OER activities of SA-PtCoF and control samples (Co, CoF, PtCo, and Pt/C@RuO_2). (a) ORR polarization curves recorded in an O_2-saturated electrolyte at 1600 rpm and 5 mV s^{-1}. (b) ORR polarization curves of SA-PtCoF at different rotating speeds. (c) Koutechy–Levich (K–L) plots for all samples at 0.65 V. (d) OER polarization curves at 1600 rpm and 5 mV s^{-1} and (e) corresponding Tafel plots. (f) Overall bifunctional ORR/OER performances. The bifunctional ORR/OER activities are verified by the potential difference between half-wave potentials for the ORR derived from (a) and the potentials for the OER at 10 mA cm^{-2} derived from (d).

of 0.6 V is recorded for SA-PtCoF, suggesting the superior ORR kinetics. Electrochemical impedance spectroscopy (EIS) images of SA-PtCoF show a smaller semicircle than that of PtCo, implying facilitated charge transfer (Fig. S14, ESI†). Moreover, electrochemical active surface area (EASA, determined by the double-layer capacitance, Fig. S15, ESI†) of SA-PtCoF (0.159 mF cm^{-2}) is much higher than those of Co (0.082 mF cm^{-2}), CoF (0.111 mF cm^{-2}), and PtCo (0.126 mF cm^{-2}), implying more electrochemically active surfaces created after forming stabilized atomic Pt by F-plasma treatment. In addition, the limited current densities under different rotation speeds and the corresponding Koutecky–Levich (K–L) plots of SA-PtCoF and control samples are examined in Fig. 4b, c and Fig. S16, S17 (ESI†). The number of electrons transferred (n) in the case of SA-PtCoF was calculated to be almost 4.0 in a potential range of 0.55–0.75 V, confirming a high-efficiency ORR at a low overpotential.

Besides supreme ORR activity, the SA-PtCoF catalyst also exhibits an excellent OER performance to receive 10 mA cm^{-2} current density at an overpotential of 308 mV (Fig. 4d), which is much lower than those of other control catalysts (Co at 337 mV, CoF at 329 mV, PtCo at 323 mV, and Pt/C@RuO_2 at 416 mV). The electron-donating Co in the alloyed matrix serves as active sites, affecting the electronic environment by Pt incorporation and thus facilitating the OH^- adsorption for the OER.[34,38] Additionally, the trapped interstitial F induces slight lattice distortion (Fig. 2d), generating dangling bonds and further enhancing the OER activity.[23,52,53] The OER kinetics for the catalysts were studied by Tafel plots (Fig. 4e). SA-PtCoF displays a Tafel slope of 68 mV dec^{-1}, which is much smaller than those of PtCo (87 mV dec^{-1}), CoF (111 mV dec^{-1}), and Co (123 mV dec^{-1}). It proves that SA-PtCoF is favorable for OER kinetics due to the enriched active sites for oxygen-related intermediate absorption. Chronoamperometry tests of SA-PtCoF (Fig. S18, ESI†) were also employed to investigate the catalyst stability at 2 mA cm^{-2} (ORR) and 10 mA cm^{-2} (OER) for 25 h, which show very stable ORR/OER activity during long-term testing. By contrast, the Pt/C@RuO_2 electrode shows significant changes in ORR/OER potentials during the stability test. Furthermore, the potential difference between the ORR and OER under 25 h operation shows almost no change for SA-PtCoF but an increase of 0.025 V for Pt/C@RuO_2. It implies that the SA-PtCoF catalyst delivers supreme activity and stability for both ORR and OER. Additionally, we tested the stability of SA-PtCoF by CV over long periods of time. The final phase of SA-PtCoF was investigated by XRD (Fig. S19, ESI†), revealing that metallic Co is still the main phase in the catalysts as compared with the fresh catalyst before the stability test. It confirms the structural stability of SA-PtCoF for electrochemical applications. Furthermore, the morphology of SA-PtCoF after the stability test characterized by SEM (Fig. S20a, ESI†) shows that the catalysts maintain a similar morphology to the fresh samples, revealing the excellent morphological stability and robust nanostructure of SA-PtCoF. The HAADF-STEM (Fig. S20b, ESI†) further proves that the Pt active sites are atomically dispersed in the PtCoF matrix, indicating the strong interaction between the Pt atoms and the PtCoF matrix, which is consistent with the result of *ex situ* XAS (Fig. S21, ESI†). In addition, XAS measurements (Fig. S21, ESI†) demonstrate no change in the oxidization state and local structure of Pt after the stability test, confirming that the Pt atoms are stable in the SA-PtCoF catalyst. As shown in Table S4 (ESI†), there is no significant weight percentage change of Pt in the SA-PtCoF, further verifying that Pt is well stabilized in the nanosheet without falling off into the electrolyte during the stability test. Moreover, the ABF-TEM image (Fig. S20c, ESI†) illustrates that a thin layer of hydroxylated Co layer is formed at the edge of PtCoF when compared with the as-prepared SA-PtCoF before the test (Fig. S2c, ESI†). Note that the metallic Co on the surface is generally prone to be partially hydroxylated, which is normal in the Co-based catalysts and favorable not only to prevent the metallic Co from further oxidization but also to provide more active sites for the enhanced catalytic activity.[54]

The bifunctional ORR/OER activities of all control catalysts were also examined by estimating the potential difference between $E_{1/2}$ for the ORR and potential at 10 mA cm^{-2} for the OER recorded in the LSV curves (Fig. 4f). Obviously, the minimal potential difference of 658 mV is achieved from the SA-PtCoF catalyst, which is superior to the control samples (887 mV for Co, 819 mV for CoF, and 693 mV for PtCo) and commercial Pt/C-RuO_2 (781 mV). Additionally, it outperforms the state-of-the-art catalysts as summarized in Table S5 (ESI†). In order to assess the effects of Pt loading on the ORR/OER activity, PtCoF prepared from different concentrations of Pt precursors was studied by LSV measurements (Fig. S22, ESI†). The result reveals that SA-PtCoF exhibits the best ORR/OER performance among all catalysts. In addition, the electrochemical ORR/OER performance of SA-PtCoF fabricated from the different batches were tested (Fig. S23, ESI†) in order to verify the excellent repeatability of the fabrication route. Specifically, four SA-PtCoF catalysts fabricated at different times show almost the same ORR activity, including the onset potential, half-wave potential, and limiting current. Meanwhile, when used for OER tests, the SA-PtCoF catalysts show repeatable activity, specifically with the onset potentials of 1.50 V and overpotentials of 310 mV at a current density of 10 mA cm^{-2}.

Importantly, the electrocatalytic mechanism of SA-PtCoF was discussed by the investigation of the reaction intermediates during the ORR and OER through *ex situ* Raman spectra measurements (Fig. S24, ESI†). Note that the metallic Pt and Co are inactive in the Raman spectra, which may not provide solid evidence for the surface composition change if the metallic phase is the active site in the catalytic reaction such as the ORR. After the ORR/OER cycling test, an intensive peak at 500 cm^{-1} and a weaker peak centered at 628 cm^{-1} are identified as CoOOH. However, there is no evidence of Pt–O formation from the Raman spectra, indicating that Pt atoms are stable without oxidizing during catalytic reactions.[55,56] The metallic Co phase in the SA-PtCoF will be partially oxidized to CoOOH in an alkaline solution during the OER, which has been well accepted in Co-based catalysts.[54] Moreover, the CoOOH phase is mostly recognized as the active sites for the OER due to the accelerated

formation of molecular oxygen by oxidizing the absorbed OH^- in the alkaline solution. In terms of the ORR process, three possible oxygen dissociation pathways would take place, including oxygen molecular dissociation, hydrogen peroxide dissociation, and peroxyl dissociation.[3,57,58] In this work, the ORR mechanism of SA-PtCoF follows the peroxyl dissociation pathway. The absorbed oxygen molecule on the surface of SA-PtCoF is reduced to HOO*, which is further dissociated into O* and OH*. The intermediates will be eventually reduced to water molecules. All these processes will be completed *via* a four-electron transfer pathway. Note that the d-band center of Pt in the SA-PtCoF is downshifted *via* transition metals such as Co, which has been confirmed by XPS (Fig. 2c and d). For the ORR, the downshift of the d-band center of Pt leads to weak adsorption of the intermediates such as atomic oxygen, hydroxyl, and peroxyl because of the strong electrostatic repulsion, which facilitates the oxygen reduction.[58]

In addition to the outstanding electrochemical ORR/OER activity, SA-PtCoF was also used as an air cathode to investigate its practical application in rechargeable ZABs. The galvanostatic charge/discharge profile (Fig. 5a) was recorded at a current density of 10 mA cm^{-2} for SA-PtCoF and Pt/C@RuO_2. As compared with Pt/C@RuO_2, the SA-PtCoF catalyst possesses a smaller voltage gap during charge/discharge cycling. After cycling for 240 h, the voltage gap for SA-PtCoF reduces greatly from 1.03 V to 0.9 V, indicating an activation process during cycling, while the commercial Pt/C@RuO_2 electrodes show an increased voltage gap from 0.69 V to 1.03 V, meaning a catalyst degradation. Moreover, to verify SA-PtCoF as an ideal cathode material in the ZAB with superior durability for long cycling,

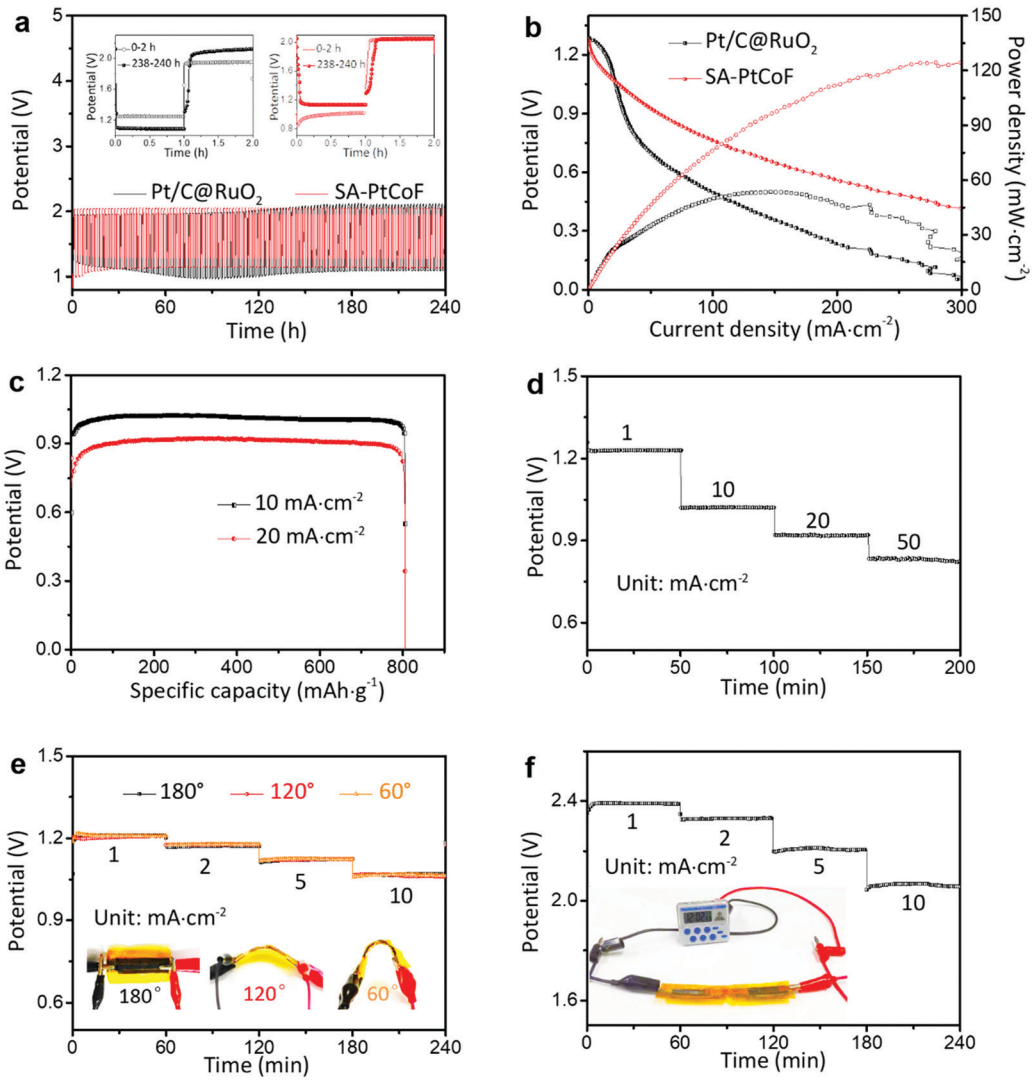

Fig. 5 ZAB performance using the SA-PtCoF cathode. (a) Long-term discharge/charge curves of SA-PtCoF and Pt/C@RuO_2 at a current density of 10 mA cm^{-2}. The inset shows the corresponding first and last discharge/charge profiles. (b) Polarization curves of SA-PtCoF and Pt/C@RuO_2 in the ZAB. (c) Long-term discharge curves of the ZAB using the SA-PtCoF cathode at different current densities. The specific capacity was calculated based on the mass consumption of Zn. (d) Typical galvanostatic discharge curves of the ZAB using the SA-PtCoF cathode at different current densities. (e and f) Galvanostatic discharge curves of a single flexible ZAB and two flexible ZAB tandem cells, respectively, at different current densities under bending tests.

the by-product was investigated by different materials characterization techniques as shown in Fig. S25 (ESI†). A very thin cobalt hydroxide layer formed on the surface of SA-PtCoF after the ZAB discharge/charge cycling (Fig. S25a, ESI†), which agreed well with the previous stability tests by CV.[54] Furthermore, the HAADF-STEM image of the SA-PtCoF catalyst after cycling (Fig. S25b, ESI†) clearly shows that the single Pt atoms are well stabilized in the PtCoF matrix. Moreover, the Pt atoms are almost stabilized atomically in the matrix, consistent with the as-prepared (uncycled) catalysts (Fig. 1e and Fig. S3a, ESI†). The high-resolution XPS Pt 4f spectra of SA-PtCoF after ZAB cycling show that metallic Pt still exists in the SA-PtCoF without being oxidized, agreeing well with the *ex situ* XAS results (Fig. S26, ESI†). Additionally, the Pt content remains constant as compared to the as-prepared SA-PtCoF (Table S4, ESI†), suggesting good stability of Pt during ZAB testing. Furthermore, XRD patterns of the cycled SA-PtCoF (Fig. S25c, ESI†) show that two peaks representing metallic Co become weaker after ZAB testing, suggesting the surface hydroxylation of Co. However, the main phase of Co in the SA-PtCoF after ZAB cycling remains unchanged, demonstrating the superior stability of the material. The EDS elemental mapping (Fig. S25d, ESI†) shows that the Co, Pt, and F elements are the main components in the SA-PtCoF, whereas, the oxygen element is also present due to the formation of Co hydroxide. Raman spectra (Fig. S27, ESI†) only show the formation of CoOOH at 497 cm^{-1} and 626 cm^{-2}, which confirms the good stability of Pt without oxidation in the SA-PtCoF.

The polarization and power density profiles (Fig. 5b) show that SA-PtCoF exhibits a maximal power density of 125 mW cm^{-2} at 266 mA cm^{-2}, much higher than those of commercial Pt/C@RuO_2 (55 mW cm^{-2} at 155 mA cm^{-2}) and other benchmark ZABs as summarized in Table S5 (ESI†). It should be highlighted that the excellent ZAB performance of SA-PtCoF can be attributed to the sufficiently exposed atomic Pt stabilized on the functional PtCoF matrix.[3,59] Moreover, the galvanostatic discharge curves of the ZAB using the SA-PtCoF cathode (Fig. 5d) do not have obvious voltage decay until the Zn anode was fully consumed, suggesting excellent durability. The specific capacity was calculated to be 808 mA h g_{Zn}^{-1} at 10 mA cm^{-2} and 806 mA h g_{Zn}^{-1} at 20 mA cm^{-2}, which are superior to those of the state-of-the-art electrodes.[60–63] The energy density of SA-PtCoF was calculated to be 785 W h kg_{Zn}^{-1} at a current density of 10 mA cm^{-2}, which is superior to those of the reported state-of-the-art counterparts.[64,65] Furthermore, the rate performance of the SA-PtCoF cathode was studied at different current densities from 1 mA cm^{-2} to 50 mA cm^{-2} (Fig. 5d). The voltage of the SA-PtCoF cathode remains very stable even at high current densities of 20 mA cm^{-2} (0.92 V) and 50 mA cm^{-2} (0.84 V). We also assembled a flexible rechargeable ZAB (Fig. S28, ESI†) consisting of the SA-PtCoF cathode, Zn anode, and an alkaline gel electrolyte. It shows an open-circuit potential (OCP) of 1.31 V in an ambient atmosphere (Fig. S29, ESI†), revealing a superior electrocatalytic activity even in an open cell system.[3] To further examine the stability under bending tests, the flexible ZAB was discharged at different current densities (Fig. 5e). There is almost no discharge voltage decay under the deformation condition at different current densities, suggesting its excellent stability and flexibility for wearable electronic applications. Moreover, the flexible ZAB can be simply stacked in tandem cells, which show approximately doubled voltages and provide sufficient voltage to light up a timer (Fig. 5f).

3. Conclusion

In summary, we rationally designed a transformative strategy to stabilize atomic Pt on alloyed PtCoF nanosheets with trapped interstitial F for rechargeable ZABs. The interstitial F atoms induce lattice distortion in the alloyed PtCoF matrix, weakening the Pt–Co bond, stabilizing the surface Pt single atoms, and eventually enhancing the utilization efficiency of Pt. As a result, the SA-PtCoF catalyst shows outstanding bifunctional ORR/OER activity, which can be attributed to the catalyst–support interactions and synergistic effects between atomic Pt and the alloyed PtCoF matrix. At the level of practical implementation, the SA-PtCoF catalyst as a cathode in a ZAB can be cycled for over 240 h with a peak power density of 125 mW cm^{-2} and a specific capacity of 808 mA h g_{Zn}^{-1} at 10 mA cm^{-2}. As a proof-of-concept, the SA-PtCoF catalyst was also assembled into a flexible ZAB for wearable electronics. Overall, this work will open a new paradigm for stabilizing atomic catalysts on alloyed supports as high-efficiency electrocatalysts in the field of energy conversion and storage.

Author contributions

Z. L., W. N., and Z. Y. contributed equally to this work. Y. Y., Z. L., and W. N. designed the experiments. Z. L. synthesized and characterized the material. Z. Y. carried out the TEM analysis under the direction of Y. D. N. Z. and A. K. performed the DFT calculation and wrote the corresponding DFT section. G. E. S., W. S., M. V. V., M. W., H. C., H. Z., and Z. F. performed XAS analyses and wrote the corresponding XAS section. Z. L. analyzed the data and wrote the manuscript. Y. Y. oversaw all results and corrected the manuscript. All authors approved the manuscript.

Conflicts of interest

There are no conflicts to declare.

Acknowledgements

This work was supported by the National Science Foundation under Grant No. CMMI-1851674 and the startup grant from the University of Central Florida. Y. Y. thanks Prof. Nina Orlovskaya at the University of Central Florida for help with the Raman spectrum analysis. Z. F. thanks Oregon State University for the startup support. W. S. acknowledges the support from PNNL-OSU Distinguished Graduate Fellowship. TEM and data analysis were supported by the U.S. Department of Energy, Office of Science, Office of Basic Energy Sciences, Early Career Research Program under award # 68278. A portion of the

research was performed using EMSL, a DOE User Facility sponsored by the Office of Biological and Environmental Research and located at the Pacific Northwest National Laboratory. The use of the Advanced Photon Source at Argonne National Laboratory for XAS measurements at beamlines 20-BM and 9-BM was supported by the U.S. Department of Energy under contract no. DE-AC02-06CH11357.

References

1 J. Fu, Z. P. Cano, M. G. Park, A. Yu, M. Fowler and Z. Chen, *Adv. Mater.*, 2017, **29**, 1604285.
2 L. Guo, J. Deng, G. Wang, Y. Hao, K. Bi, X. Wang and Y. Yang, *Adv. Funct. Mater.*, 2018, **28**, 1804540.
3 W. Niu, S. Pakhira, K. Marcus, Z. Li, J. L. Mendoza-Cortes and Y. Yang, *Adv. Energy Mater.*, 2018, **8**, 1800480.
4 Y. J. Wang, N. Zhao, B. Fang, H. Li, X. T. Bi and H. Wang, *Chem. Rev.*, 2015, **115**, 3433–3467.
5 X.-M. Li, M.-H. Bi, L. Cui, Y.-Z. Zhou, X.-W. Du, S.-Z. Qiao and J. Yang, *Adv. Funct. Mater.*, 2017, **27**, 1605703.
6 T. Reier, M. Oezaslan and P. Strasser, *ACS Catal.*, 2012, **2**, 1765–1772.
7 W. Niu, L. Li, N. Wang, S. Zeng, J. Liu, D. Zhao and S. Chen, *J. Mater. Chem. A*, 2016, **4**, 10820–10827.
8 D. Wang, H. L. Xin, R. Hovden, H. Wang, Y. Yu, D. A. Muller, F. J. DiSalvo and H. D. Abruna, *Nat. Mater.*, 2013, **12**, 81–87.
9 Y. Zhang, C. Wu, H. Jiang, Y. Lin, H. Liu, Q. He, S. Chen, T. Duan and L. Song, *Adv. Mater.*, 2018, **30**, e1707522.
10 H. Zhang, P. An, W. Zhou, B. Y. Guan, P. Zhang, J. Dong and X. W. D. Lou, *Sci. Adv.*, 2018, **4**, eaao6657.
11 L. Ma, S. Chen, Z. Pei, Y. Huang, G. Liang, F. Mo, Q. Yang, J. Su, Y. Gao, J. A. Zapien and C. Zhi, *ACS Nano*, 2018, **12**, 1949–1958.
12 W. Zang, A. Sumboja, Y. Ma, H. Zhang, Y. Wu, S. Wu, H. Wu, Z. Liu, C. Guan, J. Wang and S. J. Pennycook, *ACS Catal.*, 2018, **8**, 8961–8969.
13 R. Lang, W. Xi, J. C. Liu, Y. T. Cui, T. Li, A. F. Lee, F. Chen, Y. Chen, L. Li, L. Li, J. Lin, S. Miao, X. Liu, A. Q. Wang, X. Wang, J. Luo, B. Qiao, J. Li and T. Zhang, *Nat. Commun.*, 2019, **10**, 234.
14 Y. Peng, Z. Geng, S. Zhao, L. Wang, H. Li, X. Wang, X. Zheng, J. Zhu, Z. Li, R. Si and J. Zeng, *Nano Lett.*, 2018, **18**, 3785–3791.
15 T. Chao, X. Luo, W. Chen, B. Jiang, J. Ge, Y. Lin, G. Wu, X. Wang, Y. Hu, Z. Zhuang, Y. Wu, X. Hong and Y. Li, *Angew. Chem., Int. Ed.*, 2017, **56**, 16047–16051.
16 G. Wang, B. Huang, L. Xiao, Z. Ren, H. Chen, D. Wang, H. D. Abruna, J. Lu and L. Zhuang, *J. Am. Chem. Soc.*, 2014, **136**, 9643–9649.
17 Y. Nie, L. Li and Z. Wei, *Chem. Soc. Rev.*, 2015, **44**, 2168–2201.
18 H. H. Shin, L. Lu, Z. Yang, C. J. Kiely and S. McIntosh, *ACS Catal.*, 2016, **6**, 2811–2818.
19 S. Liang, C. Hao and Y. Shi, *ChemCatChem*, 2015, **7**, 2559–2567.
20 H. Zhang, G. Liu, L. Shi and J. Ye, *Adv. Energy Mater.*, 2018, **8**, 1701343.
21 C. Wang, Y. Liu and T. Suga, *ECS Trans.*, 2016, **75**, 153–161.
22 C. Zhang, Y. Shi, Y. Yu, Y. Du and B. Zhang, *ACS Catal.*, 2018, **8**, 8077–8083.
23 J. Yang, Z.-A. Ren, G.-C. Che, W. Lu, X.-L. Shen, Z.-C. Li, W. Yi, X.-L. Dong, L.-L. Sun, F. Zhou and Z.-X. Zhao, *Supercond. Sci. Technol.*, 2009, **22**, 025004.
24 A. Cullis, *MRS Bull.*, 1996, **21**, 21–26.
25 M. Scheffler and J. Dabrowski, *Philos. Mag. A*, 1988, **58**, 107–121.
26 J. Dong, H. J. Zhang, G. Xu, Z. Li, G. Li, W. Z. Hu, D. Wu, G. F. Chen, X. Dai, J. L. Luo, Z. Fang and N. L. Wang, *Europhys. Lett.*, 2008, **83**, 27006.
27 Z. Zhao, M. Li, L. Zhang, L. Dai and Z. Xia, *Adv. Mater.*, 2015, **27**, 6834–6840.
28 H. Zhou, F. Yu, Q. Zhu, J. Sun, F. Qin, L. Yu, J. Bao, Y. Yu, S. Chen and Z. Ren, *Energy Environ. Sci.*, 2018, **11**, 2858–2864.
29 J. Zhang, T. Wang, P. Liu, Z. Liao, S. Liu, X. Zhuang, M. Chen, E. Zschech and X. Feng, *Nat. Commun.*, 2017, **8**, 15437.
30 L. Li, S.-H. Chai, S. Dai and A. Manthiram, *Energy Environ. Sci.*, 2014, **7**, 2630.
31 G. Pattanaik and G. Zangari, *J. Electrochem. Soc.*, 2006, **153**, C6–C10.
32 S. Franz, P. L. Cavallotti, M. Bestetti, V. Sirtori and L. Lombardi, *J. Magn. Magn. Mater.*, 2004, **272–276**, 2430–2431.
33 B. J. Hwang, S. M. S. Kumar, C.-H. Chen, Monalisa, M.-Y. Cheng, D.-G. Liu and J.-F. Lee, *J. Phys. Chem. C*, 2007, **111**, 15267–15276.
34 S. Wang, S. P. Jiang, X. Wang and J. Guo, *Electrochim. Acta*, 2011, **56**, 1563–1569.
35 V. T. Ho, C. J. Pan, J. Rick, W. N. Su and B. J. Hwang, *J. Am. Chem. Soc.*, 2011, **133**, 11716–11724.
36 W. Wang, H. Wang, Y. Yu, Z. Wu, M. Asif and H. Liu, *Catal. Sci. Technol.*, 2018, **8**, 480–485.
37 J. N. Tiwari, S. Sultan, C. W. Myung, T. Yoon, N. Li, M. Ha, A. M. Harzandi, H. J. Park, D. Y. Kim, S. S. Chandrasekaran, W. G. Lee, V. Vij, H. Kang, T. J. Shin, H. S. Shin, G. Lee, Z. Lee and K. S. Kim, *Nat. Energy*, 2018, **3**, 773–782.
38 W. Niu, J. Shi, L. Ju, Z. Li, N. Orlovskaya, Y. Liu and Y. Yang, *ACS Catal.*, 2018, **8**, 12030–12040.
39 N. V. Kosova, E. T. Devyatkina and V. V. Kaichev, *J. Power Sources*, 2007, **174**, 735–740.
40 C. He, Y. Yu, X. Hu and A. Larbot, *Appl. Surf. Sci.*, 2002, **200**, 239–247.
41 V. Zardetto, F. di Giacomo, H. Lifka, M. A. Verheijen, C. H. L. Weijtens, L. E. Black, S. Veenstra, W. M. M. Kessels, R. Andriessen and M. Creatore, *Adv. Mater. Interfaces*, 2018, **5**, 1701456.
42 Z.-W. Fu, C.-L. Li, W.-Y. Liu, J. Ma, Y. Wang and Q.-Z. Qin, *J. Electrochem. Soc.*, 2005, **152**, E50–E55.
43 G. Kresse and J. Furthmüller, *Phys. Rev. B: Condens. Matter Mater. Phys.*, 1996, **54**, 11169.
44 J. P. Perdew, K. Burke and M. Ernzerhof, *Phys. Rev. Lett.*, 1996, **77**, 3865.
45 P. E. Blöchl, *Phys. Rev. B: Condens. Matter Mater. Phys.*, 1994, **50**, 17953.

46 F. Vincent and M. Figlarz, *C. R. Seances Acad. Sci., Ser. C*, 1967, **264**, 1270.
47 Z. Feng, Q. Ma, J. Lu, H. Feng, J. Elam, P. C. Stair and M. J. Bedzyk, *RSC Adv.*, 2015, **5**, 103834–103840.
48 M. Wang, B. Han, J. Deng, Y. Jiang, M. Zhou, M. Lucero, Y. Wang, Y. Chen, Z. Yang, A. T. N'Diaye, Q. Wang, Z. J. Xu and Z. Feng, *ACS Appl. Mater. Interfaces*, 2019, **11**, 5682–5686.
49 P. Li, M. Wang, X. Duan, L. Zheng, X. Cheng, Y. Zhang, Y. Kuang, Y. Li, Q. Ma and Z. Feng, *Nat. Commun.*, 2019, **10**, 1711.
50 K. Liang, S. Pakhira, Z. Yang, A. Nijamudheen, L. Ju, M. Wang, C. I. Aguirre-Velez, G. E. Sterbinsky, Y. Du and Z. Feng, *ACS Catal.*, 2018, **9**, 651–659.
51 M. Wang, L. Árnadóttir, Z. J. Xu and Z. Feng, *Nano-Micro Lett.*, 2019, **11**, 47.
52 X. Zeng, J. Shui, X. Liu, Q. Liu, Y. Li, J. Shang, L. Zheng and R. Yu, *Adv. Energy Mater.*, 2018, **8**, 1701345.
53 X. Fan, Y. Liu, S. Chen, J. Shi, J. Wang, A. Fan, W. Zan, S. Li, W. A. Goddard, 3rd and X. M. Zhang, *Nat. Commun.*, 2018, **9**, 1809.
54 P. Chen, K. Xu, Z. Fang, Y. Tong, J. Wu, X. Lu, X. Peng, H. Ding, C. Wu and Y. Xie, *Angew. Chem., Int. Ed.*, 2015, **54**, 14710–14714.
55 T. Pauporte, L. Mendoza, M. Cassir, M. C. Bernard and J. Chivot, *J. Electrochem. Soc.*, 2005, **152**, C49.
56 F. Zaccarini, G. Garuti, R. J. Bakker and E. Pushkarev, *Microsc. Microanal.*, 2015, **21**, 1070–1079.
57 X. Lv, W. Wei, H. Wang, B. Huang and Y. Dai, *Appl. Catal., B*, 2019, **255**, 117743.
58 Z. Duan and G. Wang, *Phys. Chem. Chem. Phys.*, 2011, **13**, 20178.
59 P. Chen, T. Zhou, L. Xing, K. Xu, Y. Tong, H. Xie, L. Zhang, W. Yan, W. Chu, C. Wu and Y. Xie, *Angew. Chem., Int. Ed.*, 2017, **56**, 610–614.
60 S. S. Shinde, C. H. Lee, A. Sami, D. H. Kim, S. U. Lee and J. H. Lee, *ACS Nano*, 2017, **11**, 347–357.
61 N. Xu, Q. Nie, L. Luo, C. Z. Yao, Q. Gong, Y. Liu, X. Zhou and J. Qiao, *ACS Appl. Mater. Interfaces*, 2019, **11**, 578–587.
62 Y.-J. Wang, B. Fang, D. Zhang, A. Li, D. P. Wilkinson, A. Ignaszak, L. Zhang and J. Zhang, *Electrochem. Energy Rev.*, 2018, **1**, 1–34.
63 J. F. Parker, E. S. Nelson, M. D. Wattendorf, C. N. Chervin, J. W. Long and D. R. Rolison, *ACS Appl. Mater. Interfaces*, 2014, **6**, 19471–19476.
64 Y. Li, M. Gong, Y. Liang, J. Feng, J. E. Kim, H. Wang, G. Hong, B. Zhang and H. Dai, *Nat. Commun.*, 2013, **4**, 1805.
65 J. Pan, Y. Y. Xu, H. Yang, Z. Dong, H. Liu and B. Y. Xia, *Adv. Sci.*, 2018, **5**, 1700691.

